LETTER

Three-dimensional imaging of dislocations in a nanoparticle at atomic resolution

Chien-Chun Chen[1,2]*, Chun Zhu[1,2]*, Edward R. White[1,2], Chin-Yi Chiu[2,3], M. C. Scott[1,2], B. C. Regan[1,2], Laurence D. Marks[4], Yu Huang[2,3] & Jianwei Miao[1,2]

Dislocations and their interactions strongly influence many material properties, ranging from the strength of metals and alloys to the efficiency of light-emitting diodes and laser diodes[1–4]. Several experimental methods can be used to visualize dislocations. Transmission electron microscopy (TEM) has long been used to image dislocations in materials[5–9], and high-resolution electron microscopy can reveal dislocation core structures in high detail[10], particularly in annular dark-field mode[11]. A TEM image, however, represents a two-dimensional projection of a three-dimensional (3D) object (although stereo TEM provides limited information about 3D dislocations[4]). X-ray topography can image dislocations in three dimensions, but with reduced resolution[12]. Using weak-beam dark-field TEM[13] and scanning TEM[14], electron tomography has been used to image 3D dislocations at a resolution of about five nanometres (refs 15, 16). Atom probe tomography can offer higher-resolution 3D characterization of dislocations, but requires needle-shaped samples and can detect only about 60 per cent of the atoms in a sample[17]. Here we report 3D imaging of dislocations in materials at atomic resolution by electron tomography. By applying 3D Fourier filtering together with equal-slope tomographic reconstruction, we observe nearly all the atoms in a multiply twinned platinum nanoparticle. We observed atomic steps at 3D twin boundaries and imaged the 3D core structure of edge and screw dislocations at atomic resolution. These dislocations and the atomic steps at the twin boundaries, which appear to be stress-relief mechanisms, are not visible in conventional two-dimensional projections. The ability to image 3D disordered structures such as dislocations at atomic resolution is expected to find applications in materials science, nanoscience, solid-state physics and chemistry.

Crystallographic techniques are currently the primary means for determining the 3D atomic structures of crystals. They determine atomic positions by averaging over many unit cells. As a complement to crystallographic techniques, electron tomography is an ideal technique for imaging the 3D local structure of materials at high resolution[15,16,18–20]. By combining annular dark-field scanning TEM with the centre-of-mass (CM) and equally sloped tomography (EST) methods, electron tomography has recently achieved a resolution of 2.4 Å (ref. 20) However, dynamical scattering effects[21], the missing-wedge problem[16,18,20] and Poisson noise in the tilt series introduce noise in the EST reconstruction. Consequently, although lattice structure and some individual atoms are visible in the reconstruction[20], electron tomography has not been able to reveal 3D dislocations in materials at atomic resolution. Here we overcome this obstacle by combining 3D Fourier filtering with high-angle annular dark-field scanning TEM (HAADF-STEM) tomography, and achieve 3D imaging of dislocations in a nanoparticle at atomic resolution.

Platinum (Pt) nanoparticles were synthesized by peptide sequences in aqueous solution (Methods)[22]. To make the nanoparticles more stable under an electron beam, a thin (~1–2 nm) carbon layer was deposited on the nanoparticles (Methods). Using HAADF-STEM[14], we acquired a tilt series of projections from a Pt nanoparticle (Methods). Supplementary Figs 1 and 2 show the tilt series of 104 projections with equal-slope increments and a tilt range of $\pm 72.6°$. To monitor beam-induced changes to the Pt nanoparticle, three $0°$ projections were measured while acquiring the tilt series (Supplementary Fig. 3). The consistency of these projections indicates that the lattice structure of the nanoparticle was stable throughout the experiment.

After performing background subtraction and CM alignment (Methods), the tilt series was reconstructed by the EST method[20,23–26] (Methods). Figure 1a shows the 3D Fourier transform of the reconstruction and Fig. 1c shows a 2.6-Å-thick central slice in the x–y plane,
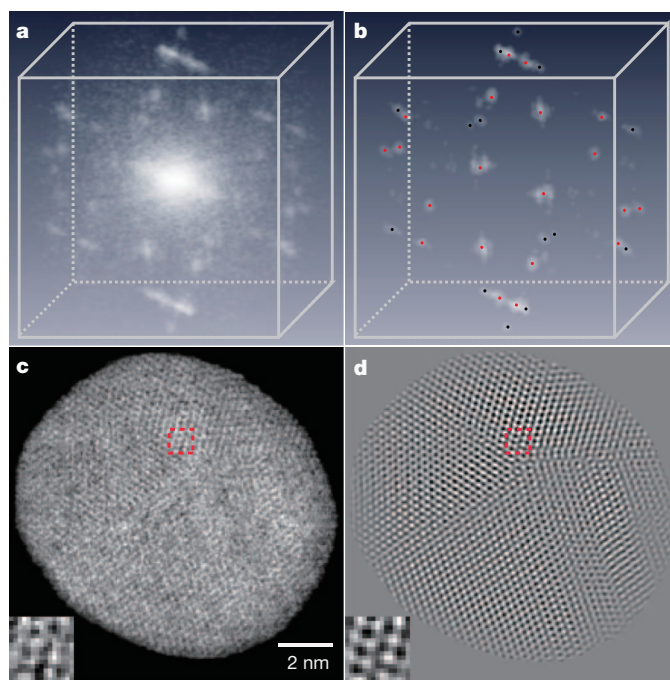

Figure 1 | 3D reconstruction of a multiply twinned Pt nanoparticle before and after applying a 3D Fourier filter. a, 3D Fourier transform of the raw reconstruction of the nanoparticle. **b**, 3D Fourier transform of the reconstruction after 3D Fourier filtering where the {111} and {200} Bragg peaks are labelled with red and black dots, respectively. **c**, A 2.6-Å-thick central slice in the x–y plane of the raw reconstruction, where the z axis is along the beam direction. **d**, The same slice of the 3D structure after applying a 3D Fourier filter, in which nearly all the atoms (in white) are visible. The clear boundary of the nanoparticle is due to the multiplication of the 3D structure with a 3D shape obtained from the EST reconstruction (Methods). The insets show an enlarged region of the atomic positions before and after applying a 3D Fourier filter.

[1]Department of Physics and Astronomy, University of California, Los Angeles, California 90095, USA. [2]California NanoSystems Institute, University of California, Los Angeles, California 90095, USA. [3]Department of Materials Science and Engineering, University of California, Los Angeles, California 90095, USA. [4]Department of Materials Science and Engineering, Northwestern University, Evanston, Illinois 60201, USA.
*These authors contributed equally to this work.

where the electron beam is along the z axis. However, owing to the low signal-to-noise ratio (SNR) in the EST reconstruction, 3D dislocations within the nanoparticle cannot be identified at atomic resolution. To enhance the SNR of the reconstruction, we developed a 3D Fourier filtering method to identify all the measurable 3D Bragg peaks and the 3D distribution around each peak (Methods). Figure 1b shows the 3D Fourier transform of the reconstruction after 3D Fourier filtering, in which the red and black dots indicate the {111} and {200} peaks of the Pt nanoparticle, respectively. By applying an inverse Fourier transform to Fig. 1b and multiplying it by the 3D shape of the Pt nanoparticle determined from the EST reconstruction, we obtained the 3D structure of the nanoparticle with a size of $\sim 11.2 \times 10.7 \times 7.1$ nm^3. Supplementary Video 1 and Fig. 1d show 3D volume renderings and a 2.6-Å-thick central slice in the x–y plane of the Pt nanoparticle, in which nearly all the atoms are visible.

To verify the 3D Fourier filtering method, we performed a comparison with a 3D Wiener filter using the same experimental data. The Wiener filter is well established for reducing the noise in a signal, and it is applied to TEM images[27]. Supplementary Fig. 5b–d shows the 2.6-Å-thick central slice in the x–y plane of the reconstruction after applying the 3D Wiener filter $S^2/(S^2 + \lambda n^2)$, where S is an estimate of the signal, n is the noise and λ is a parameter that controls the filtering strength (larger values of λ give stronger filtering). Supplementary Fig. 5f–j shows enlarged views of four regions for the raw reconstruction, and the reconstructions with the 3D Wiener filter ($\lambda = 1, 2$ and 3) and the 3D Fourier filter. Although the result with the $\lambda = 1$ Wiener filter is nosier, the atomic positions in the reconstructions using the $\lambda = 2$ and 3 Wiener filters and the 3D Fourier filter are consistent.

To further examine the 3D Fourier filtering method, we performed numerical simulations on a $7.3 \times 7.0 \times 4.5$ nm^3 decahedral Pt nanoparticle with multislice calculations. The Pt particle consists of 4,015 atoms with edge and screw dislocations (Supplementary Figs 6a–c, 7a and b). A tilt series of 63 projections with a tilt range of $\pm 72.6°$ and equal-slope increments was calculated by performing multislice STEM simulations (Supplementary Fig. 8). Two levels of Poisson noise were added to the projections of the tilt series with total electron doses of 2.52×10^5 e Å^{-2} and 5.67×10^4 e Å^{-2}, corresponding to $R_{noise} = 10\%$ and 20%, respectively, where R_{noise} is an R-factor used to define the level of Poisson noise (Methods). The two tilt series were aligned and reconstructed by the CM and EST methods[20,23–26] (Methods, Supplementary Fig. 6d–f, j–l). Because of the low SNR in the reconstructions, not all the atoms or dislocations are visible in the raw 3D reconstructions, especially with $R_{noise} = 20\%$ (Supplementary Fig. 6j–l). After applying a 3D Fourier filter to the raw reconstructions (Methods), we obtained two 3D structures of the simulated Pt nanoparticle with all the atoms resolved (Supplementary Fig. 6g–i, m–o). Furthermore, 3D grain boundaries, as well as the 3D core structures of edge and screw dislocations were determined at atomic resolution and are consistent with those in the model (Supplementary Figs 6g–i, m–o and 7c–f).

After verifying 3D Fourier filtering with a 3D Wiener filter and multislice simulation data, we analysed 3D dislocations of the Pt nanoparticle obtained from the experimental tilt series. Figure 2 shows grain boundary comparisons between a 2D experimental projection and 2.6-Å-thick internal slices of the reconstructed particle. The experimental projection in the x–y plane suggests that this is a decahedral multiply
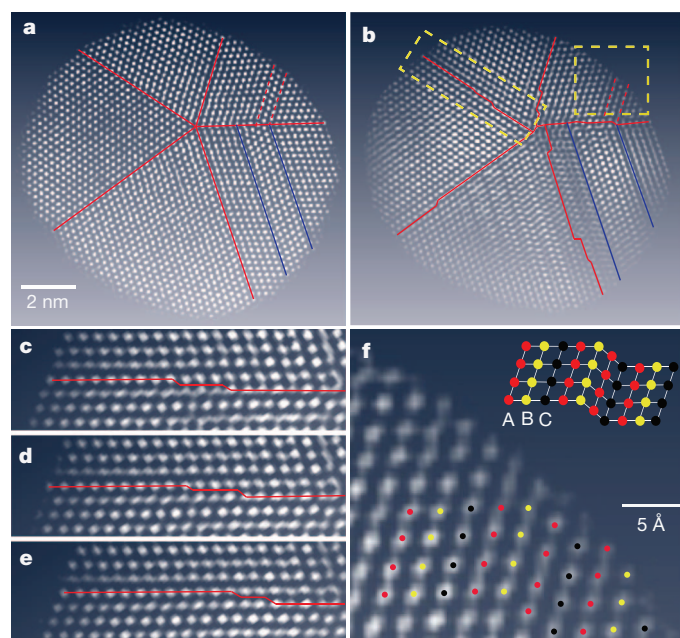

Figure 2 | Grain boundary comparisons between a 2D experimental projection and several 2.6-Å-thick internal slices of the reconstructed Pt nanoparticle. a, Experimental projection in the x–y plane suggesting that this is a decahedral multiply twinned nanoparticle and that the twin boundaries (red lines) are flat. Blue lines show two subgrain boundaries. To enhance the image contrast, a 2D Fourier filter was applied to the projection. **b**, A 2.6-Å-thick internal slice indicating the existence of atomic steps at the twin boundaries (red lines). The subgrain boundaries (blue lines) are two lattice spacings wider than those in **a**. **c**, Enlarged view of a twin boundary in **b**. **d** and **e**, a 2.6-Å-thick slice above and below the slice of **c**, revealing that the atomic steps vary in consecutive atomic layers. **f**, Enlarged view of a stacking fault in the 2.6-Å-thick internal slice, which is in good agreement with the classical model for a face-centred-cubic extrinsic stacking fault (inset). These images, as well as those in Figs 3 and 4, are displayed with Amira.
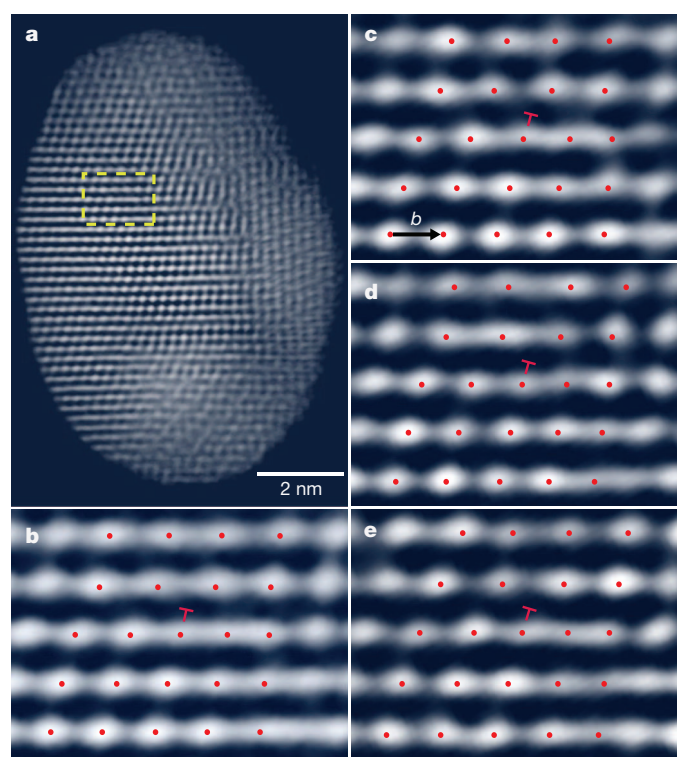

Figure 3 | Observation of the 3D core structure of an edge dislocation at atomic resolution. a, A 7.9-Å-thick internal slice of the nanoparticle. The lattice structure on the left and at the bottom parts of the slice is not well defined, mainly because this decahedral multiply twinned nanoparticle consists of five grains with different orientations. **b**, An enlarged view of an edge dislocation in **a** where red dots represent the position of the atoms. **c**, **d** and **e**, 2.6-Å-thick atomic layers sectioning through the slice of **b**. The three consecutive atomic layers indicate the dislocation line is in the direction of [10$\bar{1}$]. The Burgers vector (b) of the edge dislocation was determined to be $\frac{1}{2}$[101].

twinned nanoparticle[28] with flat twin boundaries (Fig. 2a and Supplementary Fig. 9). However, a 2.6-Å-thick internal slice in the $x–y$ plane and an enlarged view indicate the existence of atomic steps at the twin boundaries (Fig. 2b, c) that are hidden in the projection (Fig. 2a). Figure 2d and e shows enlarged views of a twin boundary in a 2.6-Å-thick slice above and below the slice of Fig. 2b, revealing that the atomic steps vary in consecutive atomic layers. These atomic steps are also independently verified by applying 3D Wiener filtering to the same experimental data (Supplementary Fig. 10). In addition, subgrain boundaries in the 2.6-Å-thick internal slice (Fig. 2b) are two lattice spacings wider than those in the projection (Fig. 2a). Figure 2f shows an enlarged view of a stacking fault in the 2.6-Å-thick internal slice ending at a twin boundary, which agrees well with the classical model for a face-centred-cubic extrinsic stacking fault[1] (inset in Fig. 2f).

In addition to twin boundaries, subgrain boundaries and stacking faults, we observed the 3D core structure of edge and screw dislocations at atomic resolution in the Pt nanoparticle. Figure 3a and b shows a 7.9-Å-thick internal slice of the nanoparticle and an enlarged view of an edge dislocation, where the red dots indicate the atomic positions. By computationally 'sectioning' the 7.9-Å-thick slice, we obtained three consecutive atomic layers, each 2.6-Å thick (Fig. 3c–e). The three consecutive atomic layers indicate that the dislocation line is in the $[10\bar{1}]$ direction, and the Burgers vector of the edge dislocation was determined to be $\frac{1}{2}[101]$ (Fig. 3c). To visualize a screw dislocation, a 5.3-Å-thick slice (two atomic layers) in the $(\bar{1}11)$ plane was selected (Supplementary Fig. 11b) and then tilted to the $[011]$ direction (Fig. 4a). Figure 4b shows an enlarged view of the slice where the zigzag pattern, a characteristic feature of a screw dislocation, is visible. To better visualize the screw dislocation, we display surface renderings of the enlarged region (Fig. 4c), where the atoms indicated by green dots are in the top layer and those indicated by red dots are in the bottom layer. The zigzag pattern is more clearly visualized in the surface renderings, in which the green line connects the atoms in the top layer and the red line connects the atoms in the bottom layer. The Burgers vector
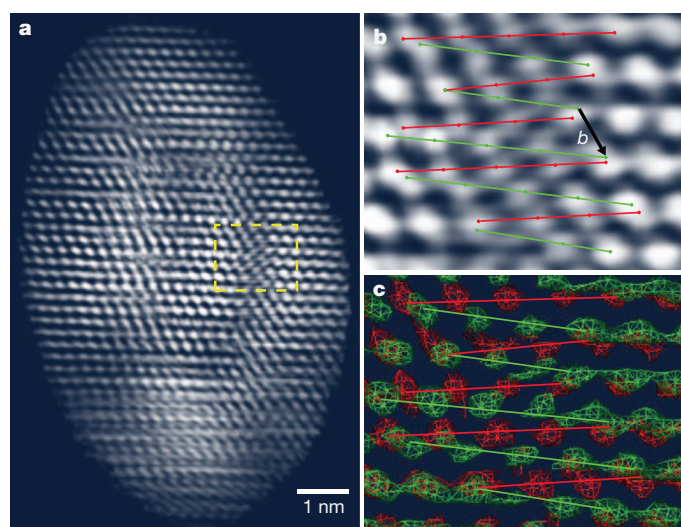
of the screw dislocation was determined to be $\frac{1}{2}[01\bar{1}]$, and the width of the screw dislocation was estimated to be ~8.9 Å, which is consistent with the results obtained by combining high-resolution TEM with image simulations for Au and Ir (ref. 29).

Careful analysis of the position of the screw dislocation inside the Pt nanoparticle suggests that the screw dislocation is associated with atomic steps at a twin boundary (Supplementary Fig. 11). Although it is often thought that nanoparticles cannot support dislocations, this is not the case for multiply twinned particles such as the decahedral one imaged here. These contain a ~2% angular strain and a disclination; at larger sizes this can in principle be relieved by dislocations[28]. A recent analysis implied that about one-third of this strain is accommodated at the twin boundaries[30], but as a 2D projection method was used in this analysis, it did not provide further insight. Our results strongly suggest that the twin boundaries are not flat and that dislocations associated with atomic steps at the boundaries account for the strain relaxation (Supplementary Fig. 11).

The significance of the present work is twofold. First, 3D atomic-resolution imaging of dislocations allows us to observe new structures that are not visible in conventional 2D projections; this is expected to advance our fundamental understanding of dislocations in materials. Second, although discrete tomography through the use of a priori information has been applied to reconstruct 3D surface morphology of a small crystalline nanoparticle at atomic resolution[31], EST-based electron tomography in combination with 3D Fourier filtering represents a general method for 3D atomic resolution imaging of the local structure in nanomaterials. Although nanoparticles are used in this study, this method could, in principle, be applied to 3D imaging of thin materials at atomic resolution; the sample thickness is limited only by dynamical electron scattering.

METHODS SUMMARY

Pt nanoparticles were synthesized by using peptide sequences in aqueous solution at room temperature[22] and supported on 5-nm-thick silicon nitride membranes. To stabilize the nanoparticles under a STEM beam, a thin (~1–2 nm) carbon layer was deposited on the Pt nanoparticles and the electron energy was kept below the knock-on radiation damage threshold of Pt. Using HAADF-STEM (energy: 200 keV; spherical aberration: 1.2 mm; illumination semi-angle: 10.7 mrad; detector inner and outer angles: 35.2 mrad and 212.3 mrad, respectively), a tilt series of 104 projections was acquired from a Pt nanoparticle with equal-slope increments[20] and a tilt range of ±72.6°. To monitor beam-induced changes to the nanoparticle, three 0° projections were measured during the acquisition of the tilt series (Supplementary Fig. 3); they indicated that the Pt nanoparticle was stable throughout the experiment. After performing background subtraction and CM alignment for the tilt series, a 3D reconstruction of the nanoparticle was obtained using the EST method[20,23–26]. However, 3D dislocations of the nanoparticle cannot be identified in the raw 3D reconstruction at atomic resolution. To enhance the SNR of the reconstruction, we developed a 3D Fourier filtering method to identify all the measurable 3D Bragg peaks and the 3D distribution around each peak. The 3D Fourier transform of the EST reconstruction consists of {111} and {200} Bragg peaks. We first determined a two-shell volume with all the measurable Bragg peaks and set other voxels to zero. We then chose the most intense {111} Bragg peak as a reference peak. After optimizing the threshold based on the reference peak (Supplementary Fig. 4) and performing convolution with a three-voxel-diameter sphere, we identified all the measurable peaks and the 3D distribution around each peak (Fig. 1b). After applying the inverse Fourier transform to Fig. 1b, the 3D structure of the Pt nanoparticle was obtained in which nearly all the atoms are visible.

Full Methods and any associated references are available in the online version of the paper.

Figure 4 | Observation of the 3D core structure of a screw dislocation at atomic resolution. a, Volume renderings of a 5.3-Å-thick slice (two atomic layers) in the $(\bar{1}11)$ plane (Supplementary Fig. 11b), tilted to the $[011]$ direction to visualize the zigzag pattern, a characteristic feature of a screw dislocation. **b**, Enlarged view of a screw dislocation showing the zigzag pattern. **c**, Surface renderings of the screw dislocation where the atoms represented by green dots are in the top layer and those by red dots are in the bottom layer. The zigzag pattern is more clearly visualized, the Burgers vector (b) of the screw dislocation was determined to be $\frac{1}{2}[01\bar{1}]$, and the width of the screw dislocation was estimated to be ~8.9 Å.

1. Hull, D. & Bacon, D. J. *Introduction to Dislocations* 5th edn (Butterworth-Heinemann, 2011).
2. Smith, W. F. & Hashemi, J. *Foundations of Materials Science and Engineering* 4th edn (McGraw-Hill Science, 2005).

3. Nakamura, S. The roles of structural imperfections in InGaN-based blue light-emitting diodes and laser diodes. *Science* **281**, 956–961 (1998).
4. Hua, G. C. *et al.* Microstructure study of a degraded pseudomorphic separate confinement heterostructure blue-green laser diode. *Appl. Phys. Lett.* **65**, 1331–1333 (1994).
5. Hirsch, P. B., Horne, R. W. & Whelan, M. J. LXVIII. Direct observations of the arrangement and motion of dislocations in aluminium. *Phil. Mag.* **1**, 677–684 (1956).
6. Bollmann, W. Interference effects in the electron microscopy of thin crystal foils. *Phys. Rev.* **103**, 1588–1589 (1956).
7. Menter, J. W. The direct study by electron microscopy of crystal lattices and their imperfections. *Proc. R. Soc. Lond. A* **236**, 119–135 (1956).
8. Howie, A. & Whelan, M. J. Diffraction contrast of electron microscope images of crystal lattice defects. III. Results and experimental confirmation of the dynamical theory of dislocation image contrast. *Proc. R. Soc. Lond. A* **267**, 206–230 (1962).
9. Hirsch, P. B., Cockayne, D. J. H., Spence, J. C. H. & Whelan, M. J. 50 years of TEM of dislocations: past, present and future. *Phil. Mag.* **86**, 4519–4528 (2006).
10. Spence, J. C. H. *Experimental High-Resolution Electron Microscopy* 3rd edn (Oxford Univ. Press, 2003).
11. Chisholm, M. F. & Pennycook, S. J. Structural origin of reduced critical currents at YBa$_2$Cu$_3$O$_{7-\delta}$ grain boundaries. *Nature* **351**, 47–49 (1991).
12. Ludwig, W. *et al.* Three-dimensional imaging of crystal defects by 'topo-tomography'. *J. Appl. Crystallogr.* **34**, 602–607 (2001).
13. Cockayne, D. J. H., Ray, I. L. F. & Whelan, M. J. Investigations of dislocation strain fields using weak beams. *Phil. Mag.* **20**, 1265–1270 (1969).
14. Pennycook, S. J. & Nellist, P. D. *Scanning Transmission Electron Microscopy: Imaging and Analysis* 1st edn (Springer, 2011).
15. Barnard, J. S., Sharp, J., Tong, J. R. & Midgley, P. A. High-resolution three-dimensional imaging of dislocations. *Science* **313**, 319 (2006).
16. Midgley, P. A. & Weyland, M. in *Scanning Transmission Electron Microscopy: Imaging and Analysis.* (eds Pennycook, S. J. & Nellist, P. D.) 353–392 (Springer, 2011).
17. Kelly, T. F. & Miller, M. K. Atom probe tomography. *Rev. Sci. Instrum.* **78**, 031101 (2007).
18. Xin, H. L., Ercius, P., Hughes, K. J., Engstrom, J. R. & Muller, D. A. Three-dimensional imaging of pore structures inside low-κ dielectrics. *Appl. Phys. Lett.* **96**, 223108 (2010).
19. Bar Sadan, M. *et al.* Toward atomic-scale bright-field electron tomography for the study of fullerene-like nanostructures. *Nano Lett.* **8**, 891–896 (2008).
20. Scott, M. C. *et al.* Electron tomography at 2.4 Å resolution. *Nature* **483**, 444–447 (2012).
21. Howie, A. Diffraction channelling of fast electrons and positrons in crystals. *Phil. Mag.* **14**, 223–237 (1966).
22. Chiu, C. Y. *et al.* Platinum nanocrystals selectively shaped using facet-specific peptide sequences. *Nature Chem.* **3**, 393–399 (2011).
23. Miao, J., Föster, F. & Levi, O. Equally sloped tomography with oversampling reconstruction. *Phys. Rev. B* **72**, 052103 (2005).
24. Lee, E. *et al.* Radiation dose reduction and image enhancement in biological imaging through equally sloped tomography. *J. Struct. Biol.* **164,** 221–227 (2008).
25. Fahimian, B. P., Mao, Y., Cloetens, P. & Miao, J. Low dose X-ray phase-contrast and absorption CT using equally-sloped tomography. *Phys. Med. Biol.* **55**, 5383–5400 (2010).
26. Zhao, Y. *et al.* High resolution, low dose phase contrast x-ray tomography for 3D diagnosis of human breast cancers. *Proc. Natl Acad. Sci. USA* **109**, 18290–18294 (2012).
27. Marks, L. D. Wiener-filter enhancement of noisy HREM images. *Ultramicroscopy* **62,** 43–52 (1996).
28. Howie, A. & Marks, L. D. Elastic strains and the energy balance for multiply twinned particles. *Phil. Mag. A* **49**, 95–109 (1984).
29. Balk, T. J. & Hemker, K. J. High resolution transmission electron microscopy of dislocation core dissociations in gold and iridium. *Phil. Mag. A* **81**, 1507–1531 (2001).
30. Johnson, C. L. J. *et al.* Effects of elastic anisotropy on strain distributions in decahedral gold nanoparticles. *Nature Mater.* **7**, 120–124 (2008).
31. Van Aert, S., Batenburg, K. J., Rossell, M. D., Erni, R. & Van Tendeloo, G. Three-dimensional atomic imaging of crystalline nanoparticles. *Nature* **470**, 374–377 (2011).

Author Contributions J.M. conceived and directed the project; C.-Y.C., C.Z., Y.H. and M.C.S. synthesized and prepared the samples; C.Z., E.R.W., B.C.R. and J.M. designed and conducted the experiments; C.-C.C. and J.M. performed the CM alignment and EST reconstruction; J.M., C.-C.C., C.Z. and L.D.M. analysed and interpreted the results, J.M., C.-C.C. and C.Z. wrote the manuscript. All authors commented on the manuscript.

Author Information Reprints and permissions information is available at www.nature.com/reprints. Our EST reconstruction software is freely available at www.physics.ucla.edu/research/imaging/EST. The authors declare no competing financial interests. Readers are welcome to comment on the online version of the paper. Correspondence and requests for materials should be addressed to J.M. (miao@physics.ucla.edu).

METHODS

Definition of R_{noise}. An R-factor was used to define the level of Poisson noise in each multislice simulation tilt series,

$$R_{noise}^{\theta} = \frac{\sum_{x,y} \left| P_{noise}^{\theta}(x,y) - P_{simulated}^{\theta}(x,y) \right|}{\sum_{x,y} P_{simulated}^{\theta}(x,y)} \quad (1)$$

where $P_{simulated}^{\theta}(x,y)$ is the projection calculated from multislice STEM simulations at angle θ, and $P_{noise}^{\theta}(x,y)$ is the same projection with Poisson noise added. After computing R_{noise}^{θ} for each projection, we calculated R_{noise} by averaging R_{noise}^{θ} for all the projections.

Synthesis of Pt nanoparticles. The Pt nanoparticles were synthesized by peptides in aqueous solution at room temperature, as reported previously[22]. All reagents were dissolved in water before using. A pre-prepared vial containing precursor (chloroplatinic acid hydrate ($H_2Pt(IV)Cl_6 \cdot xH_2O$, 1 mM) and S7 peptide (Ser–Ser–Phe–Pro–Gln–Pro–Asn) solution (30 mg ml^{-1}) were mixed with ascorbic acid (2 mM) immediately before injecting fresh $NaBH_4$ (0.8 mM), where $NaBH_4$ and ascorbic acid were used as reducing agents. The final volume of the reaction solution was 5 ml, and the reaction normally required more than 30 min.

Sample preparation. Pt nanoparticles were deposited on a 5-nm-thick silicon nitride membrane. The membrane, with a size of 100 μm × 1,500 μm, is supported on a 100-μm-thick silicon frame (http://TEMwindows.com). To dissipate charge efficiently and make the nanoparticles more stable under an electron beam, a high-temperature ultrathin carbon coating (http://TEMwindows.com) was applied to the nanoparticles based on the following procedure. The silicon nitride membrane grid was first placed in a vacuum chamber and the temperature was increased from 300 °C to 700 °C at a rate of 10 °C s^{-1}. The carbon was coated during a 5-min soak at 700 °C. The chamber then naturally cooled to 450 °C over the next 5 min before removing the grid. The silicon nitride membrane grid was finally loaded on a tomographic sample holder (Fischione 2020) for data acquisition.

Acquisition of tomographic tilt series using HAADF-STEM. STEM images of the Pt nanoparticles were acquired on a FEI Titan 80-300 microscope (energy: 200 keV; spherical aberration: 1.2 mm; illumination semi-angle, 10.7 mrad). The 100-pA electron beam was focused to a probe with a 50-μm probe-forming aperture (C2) and rastered over the sample. The scattered electrons were captured by a Fischione 3000 HAADF detector with angles between 35.2 mrad and 212.3 mrad relative to the optical axis. HAADF angles were used to reduce the nonlinear intensities and the diffraction contrast in the images. The maximum tilt angles were limited by the holder to ±75°. To reduce vibration and drift during data acquisition, the sample holder was allowed to settle for 1 h after inserting into the microscope and also for several minutes after moving to each new angle. Tilt series were manually acquired by changing the angle with equal-slope increments[20,23–26]. When focusing an image, a nearby nanoparticle (generally within 20 nm along the rotation axis) was first viewed, thus reducing unnecessary radiation dose to the particle under study[20]. Using this low-exposure acquisition scheme, a tomographic tilt series of 104 projections with equal-slope increments and a tilt range of ±72.6° was acquired from a Pt nanoparticle. The probe current was ~100 pA with a dwell time of 48 μs per pixel, and the magnification of each projection was 3.6×10^6. The total electron dose of the tilt series was estimated to be ~2.5×10^7 e Å^{-2}. Because the pixel size in STEM mode may vary, a calibration image of an oriented single-crystal Au foil (Ted Pella) was taken in STEM mode under the same conditions, and the STEM pixel size was calibrated to be 0.35 Å. To enhance the SNR in the projections of the tilt series, 1.5 × 1.5 pixel binning was performed for each projection. The pixel size of the binned projections is 0.53 Å.

Background subtraction and CM alignment. To use the EST iterative algorithm, background subtraction has to be performed for each projection. We implemented background subtraction and CM alignment based on the following procedure. First, we selected the 0° projection and chose a suitable cut-off value to subtract its background. After projecting the 0° projection onto the y axis (that is, the tilt axis) to obtain a one-dimensional (1D) curve, we calculated the centre of mass of the 1D curve (y_{CM}), and set y_{CM} as the origin of the y axis. This 1D curve was used as a reference curve. Second, we optimized the background subtraction for other projections based on the reference curve. We scanned the cut-off values from 0.5 to 1.5 times the mean value of each projection with an increment of 0.01. For each cut-off value, we projected the projection onto the y axis to obtain a 1D curve. By shifting the 1D curve pixel-by-pixel along the y axis, we calculated the difference between the 1D curve and the reference curve. We recorded the smallest difference and the corresponding shift for each 1D curve. After scanning through all the cut-off values, we plotted the smallest differences against the cut-off values, which should give a U-shaped curve. We identified the minimum corresponding to the optimized cut-off value and the shift of a given projection. After performing

background subtraction with the optimized cut-off values, we calculated the centre of mass (y_{CM}) for all the 1D curves. If all of them (that is, rounded y_{CM}) were not at the origin, we adjusted the cut-off value for the 0° projection (that is, the reference curve) and repeated the above steps until the best agreement was achieved. Finally, after performing background subtraction and aligning the projections along the y axis, we projected all the projections onto the x axis. We calculated the centre of mass (x_{CM}) for all 1D curves, and set x_{CM} as the origin of the x axis[20]. After repeating this process, all the projections were aligned to the tilt axis.

EST reconstruction. The EST iterative algorithm started with converting the measured projections to Fourier slices by the fractional Fourier transform[32]. The algorithm then iterated alternately between real and reciprocal space through the use of the pseudopolar fast Fourier transform[33]. In real space, the voxel values outside a loose support (that is, a rectangular box larger than the true boundary of the structure to be reconstructed) and the negative voxel values inside the support were set to zero, whereas in reciprocal space the corresponding calculated Fourier slices were replaced with the measured ones and the remaining slices kept unchanged in each iteration. Each iteration was monitored by an error metric, defined as the difference between the measured and calculated Fourier slices, and the algorithm was terminated after reaching a maximum number of iterations. Using the iterative EST algorithm, a preliminary 3D reconstruction was obtained after 500 iterations. An updated 3D support was determined by convolving the reconstruction with a Gaussian window and selecting a suitable cut-off. The 3D shape of the support was also double checked by examining the reconstruction slice-by-slice to ensure the support does not crop the structure. Using the updated support, we performed another 500 iterations to obtain a new reconstruction. To further improve the 3D reconstruction, we also projected the reconstruction back to calculate projections at given angles. By computing the cross-correlation between the calculated and measured projections, we further adjusted the alignment of the projections to achieve maximum consistency in 3D reconstruction. Usually the shift should be one pixel or smaller in each dimension. Otherwise, the data analysis and CM alignment procedure has to be re-done. We then repeated the procedure for improving the support and back-projection alignment. The final reconstruction was obtained when no further improvements can be made. The details of the EST algorithm can be found in refs 20, 23–26.

3D Fourier filtering. As a result of dynamical scattering effects[21], the missing-wedge problem[16,18,20] and Poisson noise in the tilt series, not all the atoms or dislocations are visible in the raw 3D EST reconstruction. To enhance the SNR in the reconstruction, we developed a 3D Fourier filtering method by using the following procedure. First, the 3D Fourier transform of the raw reconstruction of the Pt nanoparticle consists of two sets of lattice planes {111} and {200}. The intensities of the {111} peaks were estimated to be several times higher than those of the {200} peaks. We calculated the average radial distance (d) between the {111} and {200} peaks. Two radii were then determined by $R_{in} = R_{111} - d$ and $R_{out} = R_{200} + d$, where R_{111} and R_{200} are the average radial distance for the {111} and {200} peaks, respectively. By keeping those voxels in the 3D Fourier transform with their radii between R_{in} and R_{out}, and setting other voxels to zero, we obtained a two-shell volume including all the measurable 3D Bragg peaks.

Next, we implemented a method to further reduce noise among the Bragg peaks within the two-shell volume. We chose the most intense {111} Bragg peak as a reference peak and calculated thresholds based on the reference peak. We scanned the thresholds from 1% to 20% of the reference peak in steps of 1%. For each threshold, we set voxels with values larger than the threshold to one and other voxels to zero, and obtained a 3D mask. The 3D mask was convolved with a three-voxel-diameter sphere to compute a new 3D mask, where the convolution process was to retain the 3D distribution of each Bragg peak. By multiplying the new 3D mask with the Fourier transform of the raw reconstruction, we obtained a new 3D Fourier transform. By monitoring the change in the noise among the Bragg peaks, we found that a threshold with 10% of the reference peak is large enough to remove noise among the 3D Bragg peaks, while retaining all the measurable {111} and {200} peaks and the 3D distribution around each peak (Fig. 1b and Supplementary Fig. 4). The optimized threshold of 10% of the reference peak obtained here may vary for different samples.

Finally, by applying the inverse Fourier transform to Fig. 1b and multiplying it by a 3D shape (that is, a tight support) obtained from the EST reconstruction, we obtained the 3D structure of the Pt nanoparticle (Supplementary Video 1 and Fig. 1d). We confirmed the accuracy of the 3D Fourier filtering method by using two independent approaches: (1) multislice STEM simulations[34] of a decahedral Pt nanoparticle with edge and screw dislocations (Supplementary Figs 6–8) and (2) performing a comparison with a 3D Wiener filter[35] on the same experimental data (Supplementary Figs 5 and 10). In our numerical simulations, we also found that, compared to 2D Fourier filtering method[36–38], 3D Fourier filtering is more accurate. This is because in 3D Fourier filtering, each voxel in 3D reciprocal space is correlated to all voxels in 3D real space, and vice versa. But in 2D Fourier filtering,

the correlated information only exists in two dimensions. Thus, for a given object, there is more correlated information (voxels) in 3D Fourier filtering than in the 2D case.

32. Bailey, D. H. & Swarztrauber, P. N. The fractional Fourier transform and applications. *SIAM Rev.* **33,** 389–404 (1991).

33. Averbuch, A., Coifman, R. R., Donoho, D. L., Israeli, M. & Shkolnisky, Y. A framework for discrete integral transformations I — the pseudopolar Fourier transform. *SIAM J. Sci. Comput.* **30,** 785–803 (2008).

34. Kirkland, E. J. *Advanced Computing in Electron Microscopy* 2nd edn (Springer, 2010).

35. Brown, R. G. & Hwang, P. Y. C. *Introduction to Random Signals and Applied Kalman Filtering* 3rd edn (Wiley, 1996).

36. Saxton, W. O. *Computer Techniques for Image Processing in Electron Microscopy* (Academic, 1978).

37. Hawkes, P. W. *Computer Processing of Electron Microscope Images* (Springer, 1980).

38. Möbus, G., Necker, G. & Rühle, M. Adaptive Fourier-filtering technique for quantitative evaluation of high-resolution electron micrographs of interfaces. *Ultramicroscopy* **49,** 46–65 (1993).